Solid State Communications 152 (2012) 1990–1998

Contents lists available at SciVerse ScienceDirect

Solid State Communications

journal homepage: www.elsevier.com/locate/ssc

Structural transformations in chemically modified graphene ☆

Jeremy T. Robinson *,[1], Maxim K. Zalalutdinov [1], Chad E. Junkermeier [2], James C. Culbertson, Thomas L. Reinecke, Rory Stine [3], Paul E. Sheehan, Brian H. Houston, Eric S. Snow

Naval Research Laboratory, Washington, DC 20375, USA

ARTICLE INFO

Article history:
Received 9 March 2012
Accepted 12 April 2012
by L. Brey
Available online 16 July 2012

Keywords:
A. Graphene
D. Mechanical properties
A. Resonators
E. Re-crystallization

ABSTRACT

In this article, we review our efforts to continuously tune mechanical and thermal properties in multilayer chemically modified graphene (CMG) films. An alteration of the graphene lattice by functional groups, by defects created during reduction, or by defect re-crystallization is used to control CMG mechanical and thermal properties. We attribute a notable increase in Young's modulus and film strength to an emerging network of sp^2–sp^3 crosslinks established between graphene layers. Control over the film stress and strength enabled us to dramatically improve the performance of radio frequency CMG resonators by fine tuning the fabrication process.

Published by Elsevier Ltd.

1. Introduction

Carbon continues to capture the world's interest in nanoscale science and technology. Its sp^2 and sp^3 allotropes [1], and mixtures thereof, are intensely studied and are finding footholds in modern technologies. Due to continued challenges faced in forming precisely controlled carbon nanomaterials (CNMs), there remains interest in randomly assembled CNM films for commercial development and fundamental research. For example, in 2003 Snow et al. demonstrated random networks of carbon nanotubes as an electronic material [2], which found their way into thin-film transistors, chem/bio sensors [3] and transparent electrodes [4]. This same trend continues today for randomly stacked films of graphene materials and they are implemented in similar device architectures [5–7].

It is from this perspective that we consider structural transformations in randomly assembled films of graphene-based materials. While the electronic properties of such films undergo detailed study, mechanical aspects of these materials are only now becoming of broader interest [8–10]. The varied material properties in these systems derive from the amenable nature of the carbon–carbon bonds, which can produce a material that is highly conducting or insulating, transparent or opaque, or very stiff or soft. We attempt to exploit this flexible carbon chemistry to control the mechanical properties of layered sp^2 carbon in the form of graphene. In particular, we view graphene as an ideal building block to form hybrid sp^2–sp^3 bonded systems in films as thin as two atomic layers.

In this article we describe our efforts [9,11] to characterize and understand the mechanical properties of multilayer graphene-based films. We demonstrate that modifying graphene's sp^2 bonds through chemical adsorbates, together with direct crosslinking between layers, are powerful tools to engineer ultra-thin carbon materials. As assembled, these materials have an anisotropic layered character with exceptionally strong intra-layer bonding and weak (van der Waals) inter-layer interactions. Importantly, graphene's "all-surface" nature means that adatoms or defects can significantly modify its intrinsic properties. This inherent sensitivity to physical manipulation allows us to tune mechanical properties over an exceptionally wide range. This is in part due to the fact that carbon can be either an organic or inorganic material depending on functionalization and/or bonding configurations, and can have widely varying properties particularly in the mechanical domain. To appreciate the extent of the structural and mechanical metamorphosis undergone by chemically modified graphene (CMG) films, consider that such films start as sub-micron flakes with a loosely-packed structure reminiscent of paper mache. At the end of processing, they can have an elastic modulus comparable to diamond.

2. Film deposition

Established techniques to deposit/synthesize graphene materials include mechanical exfoliation [12], solution exfoliation of

☆This paper was originally an invited paper to the Solid State Communications Special Issue on Exploring Graphene, Recent Research Advances (volume 152, issue 15).

* Corresponding author.
E-mail address: Jeremy.robinson@nrl.navy.mil (J.T. Robinson).
[1] These authors contributed equally to this work.
[2] NRC Postdoctoral Fellow residing at the Naval Research laboratory.
[3] Nova Research Contractor residing at the Naval Research laboratory.

0038-1098/$ - see front matter Published by Elsevier Ltd.
http://dx.doi.org/10.1016/j.ssc.2012.04.051

graphene oxide (GO) [13], chemical vapor deposition (CVD) onto transition metals [14–16], or thermal decomposition of SiC [17]. Each approach has advantages and drawbacks, such that properties of the resulting films can vary significantly. Here we focus on the mechanical aspects of graphene materials primarily using multilayer GO, but we also use single-layer CVD graphene grown on Cu to extend the concepts to the atomic scale. We use both chemical and thermal treatments to alter the film mechanics and subsequently use micromechanical resonators to understand and characterize the structural changes within the films.

Graphene oxide deposition begins by centrifuging exfoliated GO platelets from water, isolating and re-suspending the wet solids in methanol, and then using this solution to deposit films onto SiO_2/Si or silicon-on-insulator (SOI) substrates using a modified spin-casting technique (Fig. 1a) [9]. The thinnest continuous films are approximately 1–4 monolayers thick; the thickest GO films studied here are ~50 nm. After spin-casting GO, the films are thermally treated to form reduced graphene oxide (rGO). Thermal reduction takes place in an inert atmosphere of N_2 or Ar/H_2 for temperatures ranging between 75 and 450 °C and times ranging between 1 and 24 h. The resulting rGO films have a reduced oxygen content, decreasing from an initial ~30 at% to < 10 at%. For single-layer graphene films, we use low-pressure CVD growth on Cu foils [16] and subsequently transfer graphene from Cu using wet chemical approaches [14]. This includes the use of a poly(methyl methacrylate) (PMMA) protective layer and the removal of the Cu substrate in an ammonium persulfate etchant [18].

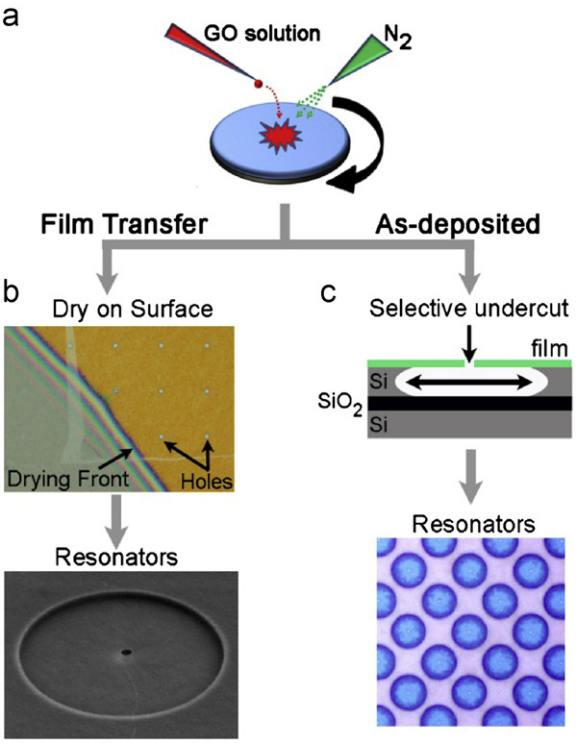

Fig. 1. (Color online) Flow chart showing the fabrication of CMG mechanical resonators: (a) deposition of GO via spin coating (adapted from [9]). (b) A GO film released in H_2O and recapture on a substrate pre-patterned with circular wells to form drum resonators. The drying front of the transferred film is labeled. A SEM image (lower panel) shows the FIB-milled hole in the center of a drum ($D \approx 3$ μm). (c) XeF_2 etching through lithographically defined holes in a CMG film on an SOI substrate. An optical microscope of resonators formed through undercutting is shown in the lower panel ($D \approx 15$ μm).

3. Suspended structures

The fabrication of suspended graphene-based structures for mechanical testing is shown in the flow chart of Fig. 1. In one process (Fig. 1b), the film is delaminated from the parent substrate, transferred into a water bath, then recaptured on a SiO_2/Si substrate pre-patterned with circular wells [9]. While this approach has a lower yield, the resultant structures remain chemically unaltered from their delaminated state. In addition, water can be trapped in the well during transfer so we use a focused ion beam (FIB) to mill a small hole in the center of the drum to release trapped gases and liquids (Fig. 1b). In the other process (Fig. 1c), we lithographically define irrigation holes through the film and selectively undercut a sacrificial silicon layer using XeF_2 gas in a Xactix® etching system [11,19]. The membrane yield using this top-down process is close to 100%. However, unlike the liquid-transfer process, the XeF_2 gas fluorinates the graphene [19] between 30 and 40 at% here, allowing us to examine the impact of fluorination on the mechanical properties.

4. Methods

4.1. Nanomechanical resonators for testing thin film mechanical properties

A portion of the suspended film that is free to vibrate and demonstrates a ring-down time in excess of a few periods of free oscillation (i.e., quality factor $Q > 10$) deserves the title "mechanical resonator". Importantly, using mechanical resonators we can extract key mechanical properties of the material from the geometry and the dynamic response of the vibrating structure. For the stress-free film the spring constant of the resonator (e.g., plate, bar, shell) is defined by the bending rigidity and thus by the material stiffness (i.e., Young's modulus, E). The presence of tension (T) can significantly alter the fundamental frequency (f_o) of the suspended structure (e.g., string or membrane). Instead of f_o being proportional to the square-root of Young's modulus, the response of highly-tensed membrane resonators is defined by the in-plane stress (σ), which allows detailed studies of stress relaxation phenomena in the membrane.

To probe the mechanical properties of suspended membrane or cantilever resonators, we use the well-established technique of laser interferometry [20,21]. A schematic of the optical setup is shown in Fig. 2. An objective lens focuses two laser beams into ~1 μm diameter spots on a sample inside a vacuum chamber

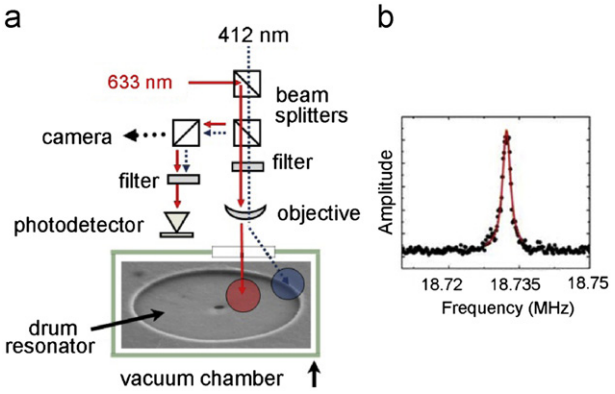

Fig. 2. (Color online) (a) Schematic showing the major components on the optical pump-probe setup used to measure the vibratory response of micromechanical resonators. The red laser is the "readout" beam; the blue laser is the "drive" beam. (b) Example of the spectral response of the fundamental mode for a drum resonator.

(pressure $< 10^{-7}$ Torr). The red laser beam ($\lambda = 633$ nm) was equipped with motorized steering mirrors that allow independent positioning of its spot within the 60×60 μm^2 image frame of a CCD camera. The optical path of the blue laser ($\lambda = 412$ nm) was fixed and its focused spot was positioned using a motorized linear stage, which moves the entire vacuum chamber. A point-like thermoelastic excitation was generated by focusing this blue laser on a single suspended resonator while modulating the power ($P < 100$ μW). This time-variable local heating modulates the film stress due to thermal expansion and can activate mechanical motion. The resulting oscillation of the resonators was detected interferometrically with the red CW laser, by measuring the modulation of the reflectivity using a wideband photodetector with a 633 nm bandpass filter. This modulation originates from the motion-induced variation of the gap in a Fabry–Perot interferometer created by the membrane (acting as a semitransparent mirror) and the underlying substrate. An example of a spectrum is shown in Fig. 2b.

For the circular drum resonators studied here, the fundamental frequency and mode spacings depend on the tension in the drum which can act either as a plate ($T \approx 0$) or as a membrane ($T \gg 0$). When under tension the drum frequencies follow a membrane behavior given by [22]

$$f_{mn} = \frac{1}{D}\sqrt{\frac{T}{\rho h}}\beta_{mn} \tag{1}$$

where h is the film thickness, D is the drum diameter, ρ is the material density, and β_{nm} is the nth root of the mth-order Bessel function. From the membrane tension and film thickness, it is straightforward to calculate the internal stress (σ) when $T > 0$ through: $\sigma = T/h$. From Eq. (1), this can be re-written as

$$\sigma = \frac{T_N}{h} = \frac{f_{nm}^2 D^2}{\beta_{nm}^2}\rho \tag{2}$$

where $\beta_{01} = 0.7655$ for the fundamental mode. We note that it is not necessary to know film thickness when calculating σ from the frequency response of the drum resonators. In the absences of tension, the frequency response is determined by the bending rigidity. For a circular plate the frequency modes are given by [23]

$$f_{mn} = \frac{\pi h}{D^2}\sqrt{\frac{E}{3\rho(1-s^2)}}(\beta_{mn})^2 \tag{3}$$

where s is Poisson's ratio and $\beta_{01} = 1.015$ for the fundamental mode. For resonators fabricated using both techniques (Fig. 1b and c), the size and position of the central hole in the resonator has a minor effect on the fundamental drum acoustics as described elsewhere [9]. The frequency response of cantilevers, which are tension free, follow a behavior described by

$$f = A\sqrt{\frac{E}{\rho}}\frac{h}{L^2} \tag{4}$$

where L is the length and $A = 0.162$ for the fundamental mode [24].

In some experiments here, through thermal anneal, the drum resonators are converted into dome-like or shell-like structures. The resonant frequencies of these relaxed domes deviate from the flat plate approximation (Eq. (3)) and as such, we use finite element modeling (FEM) to separate shape-related contributions to the resonant frequency from the contribution of the material's elastic properties. The 3D map acquired from the topographic atomic force microscopy (AFM) image of a dome was used to define the nodes of shell-type elements for the finite element model. We then use modal analysis (ANSYS FEM simulation software) to produce a set of resonant frequencies assuming a homogeneous thickness and given set of elastic properties. The fact that the fundamental frequency of shallow dome-type structures is mostly determined by the in-plane Young's modulus allows us to use an isotropic material model. We then used E as a fitting parameter to match the results of the modal analysis with the experimental value for f_o.

4.2. Thermal modeling

The power of the laser beam focused on the nanomechanical structures can be increased up to 25 mW (Fig. 2). For suspended structures, such high powers result in local high temperatures easily exceeding 1000 °C. We estimate the temperature distribution within the suspended membrane under laser exposure using FEM. We calculate the thermal conductivity (κ) of resonators by measuring how their resonance frequency changes with the readout laser power. As the measurement beam heats up the resonator, its fundamental frequency will change depending on its temperature and thermal expansion coefficient (α; TEC). The relative change in drum's frequency with heating depends on the resulting change in strain and can be written as

$$\frac{f}{f_o} = \sqrt{\frac{\varepsilon_o + \varepsilon_{laser}}{\varepsilon_o}} \tag{5}$$

where ε_o is the initial strain and ε_{laser} is strain arising from thermal expansion or contraction due to the laser heating. For a laser beam located at the center of the drum of radius R, the ε_{laser} can be estimated as the combined effect of the spatial temperature distribution $T(r)$ and temperature-dependent TEC ($\alpha(T)$):

$$\varepsilon_{laser} = \frac{1}{R^2}\int^R r\,dr \int_{Tframe}^{T(r)} \alpha(T)dT \tag{6}$$

4.3. Stress relaxation experiments

The negative thermal expansion coefficient (TEC) of graphene ($\alpha_{graphene} \approx -7 \times 10^{-6}$/K at 300 K) [25] provides an effective tool for evaluating the temperature-dependent strength of suspended films. A temperature increase results in a contracting CMG membrane and expanding silicon support frame ($\alpha_{Si} \approx 3 \times 10^{-6}$/K) and mimics stress relaxation experiments for studying viscoelastic materials [26]. The resilience (i.e., the ability to withstand high tensile stress at elevated temperature) of the resonators is characterized by thermally treating samples at a given temperature for extended times, or by treating samples for a given time at increasing temperatures. After each thermal treatment, the fundamental resonance mode is measured at RT and the resulting film stress (at RT) is calculated.

5. Results and discussion

Graphene's in-plane stiffness is comparable to that of diamond (1 TPa) [21,27] and arises from the strong sp^2-carbon bonding. In comparison, the out-of-plane shear modulus of multi-layer graphene is significantly lower than in diamond (~10 GPa for graphite) due to weak inter-layer bonding [27]. The introduction of adsorbates or defects additionally softens the in-plane Young's modulus as bonds rearrange into sp^3 configurations. This trend is clearly observed in multi-layer CMG drums formed via the liquid-transfer (Fig. 1b) or the XeF_2 undercut techniques (Fig. 1c), whose Young's moduli are typically less than 200 GPa. In addition, the Yield strength is also low, so any tensile stress in CMG drums readily relaxes (due to weak inter-layer bonding) under mild thermal treatment. In comparison, by re-crystallizing these

defects within the layers as well as between the layers, we find that both Young's moduli and strength are dramatically improved.

5.1. Resonator response

The frequency response of the "liquid-transferred" CMG resonators (Fig. 1b) vs. drum diameter is shown in Fig. 3a. The experimental values for the fundamental resonance frequency are significantly higher than that expected for structures vibrating in a tension-free mode (Eq. (3)), even for E as high as 1 TPa (lines in Fig. 3a). This indicates the drums are under tension (Eq. (1)), which we attribute to the liquid-transfer process pulling the drum surface slightly into the pre-etched well (from surface tension). In particular, AFM measurements (Fig. 3b inset) show the drums are uniformly depressed ~10 nm below the top surface and are clamped along the inner rim of the well. To release this built-in tension, we thermally anneal the CMG drums. The relatively weak inter-layer bonding within the films results in complete resonator relaxation into wrinkled domes due to platelet–platelet slippage [11] (Fig. 3b). The resonant frequencies of these relaxed, corrugated domes deviate from the flat plate approximation and as such, we use FEM to calculate Young's modulus (see Section 4). Fig. 3b and c show an example of the conversion of an AFM image into a node map (Fig. 3b), which is then used in the finite element model to calculate the fundamental resonance mode (Fig. 3c). Fig. 3d shows the best-match results for 16 different domes and reveals an average modulus of $E=185\pm58$ GPa [9]. This value, while smaller than that of graphene, is comparable to single-crystalline silicon.

A similar analysis can be made for the XeF_2-released resonators (Fig. 1c). Fig. 4a shows the drum diameter vs. the size of the irrigation hole (for a total 15 min exposure to XeF_2 gas; Pulse mode, $P_{XeF2}=1$ Torr). The etch rate of sacrificial Si layer is defined by the diffusion of reactants and products through the irrigation hole [28]. Comparable to the liquid-transferred resonators (Fig. 3), we find the frequency response for XeF_2-released drums can closely follow a membrane-like behavior (Eq. (1)) with $f_o \propto D^{-1}$ (Fig. 4b). From Eq. (2) we calculate the average resonator stress at $\sigma\sim33$ MPa. Here we estimate $\rho\approx2.2$ g/cm^3, which is higher than that of GO ($\rho=1.8$ g/cm^3 [8]) due to the addition of fluorine during XeF_2 exposure.

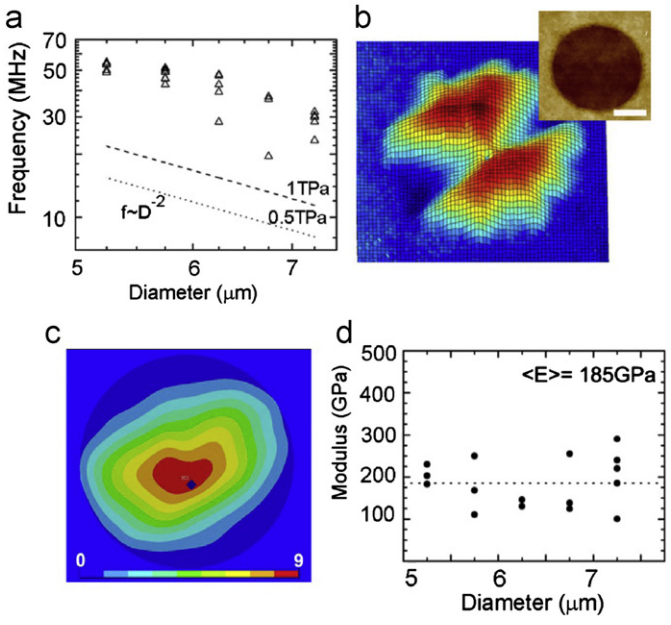

Fig. 3. (Color online) (a) Plot of resonance frequency vs. CMG drum diameter. Theoretical lines for the plate mode Eq. (3) frequencies assuming $E=1.0$ TPa and 0.5 TPa are shown. (b) Perspective AFM image of a wrinkled dome after thermal treatment (300 °C, 1 h) and stress relaxation (dome height=95 nm). (inset) AFM height image of a flat, tensioned drum before annealing. (c) FEM results for the structure shown in (b) (color scale shows out-of-plane displacement; arbitrary units) (d) Extracted Young's Modulus vs. drum diameter of relaxed CMG domes extracted from FEM (adapted from [9]).

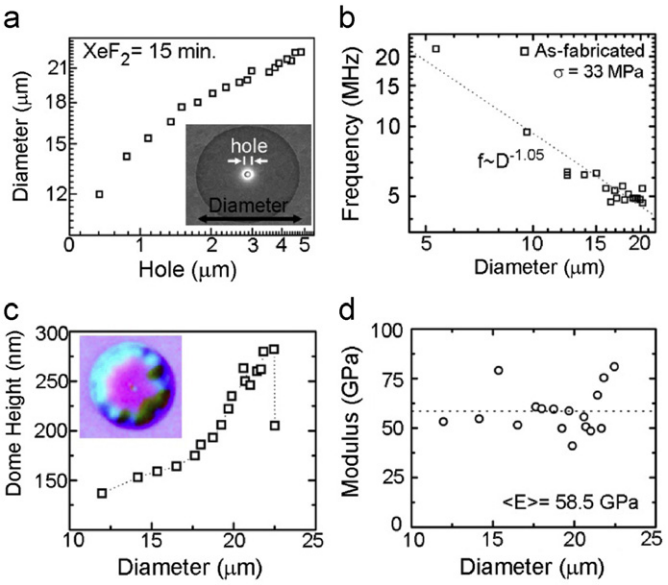

Fig. 4. (Color online) (a) Plot of drum diameter vs. irrigation hole size after a 15 min etch in XeF_2. (b) Plot of fundamental resonance frequency vs. drum diameter for as-fabricated resonators. (c) Plot of dome height vs. dome diameter for different drums annealed at 450 °C. (Inset) Nomarski optical microscope image of a 20 μm dome resonator formed after a 450 °C anneal. (d) Plot of Young's Modulus vs. dome diameter, extracted from FEM simulations.

To extract Young's modulus we relax these drum resonators via thermal annealing. A 450 °C (1 h) heat treatment of the XeF_2-released drums results in tension-free domes (Fig. 4c inset) with a fluorine content of <15 at%. In general, we find that the dome height monotonically increases with dome diameter up to a certain point ($D\approx22$ μm in Fig. 4c), above which the domes collapse into more complicated corrugated structures. In this tension-free dome state we calculate E using FEM (see Section 4), which averages ~59 GPa (Fig. 4c). This value is slightly lower than that measured for the CMG resonators in Fig. 3a, which we attribute to defects introduced during fluorine adsorption/desorption.

5.2. Defect re-crystallization: inter-platelet transformations

The previous section demonstrated that multi-layer CMG films (e.g., rGO, fluorinated rGO, etc...) have a Young's modulus notably less than graphene. This result is natural considering the relatively weak inter-platelet bonding that leads to platelet–platelet slippage and dome formation after moderate thermal annealing. The fact that exposure to fluorine followed by thermal reduction significantly decreases E of the CMG film (Fig. 3d vs. Fig. 4d) suggests that the presence of intra-platelet defects also contributes to film softening. Such residual defects within the film could include pentagon–heptagon pairs [29]; vacancies, interstitials, or Wigner defects [30]; large out-of-plane distortions [29] or free radicals, all leading to regions of quasi-amorphous sp^3 carbon [31,32] or unsaturated bonds. Importantly, carbon's ability to hybridize into various sp^2 to sp^3 configurations opens opportunities to re-crystallize these defects into new microstructures, both in-plane and out-of-plane. By measuring the fundamental

vibrational frequency of such re-crystallized resonators, we can extract the effect of a changing internal microstructure on material stiffness, in-plane stress, and film strength.

5.3. High temperature laser anneal

To induce defect re-crystallization, we use laser annealing. Laser irradiation can produce local temperatures ranging from room temperature (RT) to $>1000\,^{\circ}C$ while circumventing differences in thermal expansion between the film and substrate [25]. For example, only a few milliWatts of laser power can produce a glowing "white-hot" spot within suspended graphene-based resonators. Laser annealing is carried out using the same measurement setup described in Fig. 2, where an added green laser ($\lambda=532$ nm, ~ 1 μm spot size) is 2D rastered over the surface with powers ranging from ~ 0.1 mW to 25 mW. Fig. 5 shows screen shots taken from a movie captured as the annealing laser beam is moved across a dome resonator. Blackbody emission is observed as a bright white spot on the resonator (Fig. 5b and c). When the laser spot is closest to the drum center hole (Fig. 5b), the thermal emission has the largest diameter and intensity as compared to when the laser is at the drum edge (Fig. 5c). While we cannot currently measure the temperature of the hot spot under the laser beam (e.g. pyrometrically), we qualitatively observe similar trends between experiment (Fig. 5) and calculations (Fig. 7). By systematically annealing resonators at different laser powers and then re-measuring their frequency response, we can track how re-crystallization influences the thermal conductivity, density, modulus, and strength.

5.4. Hot spot temperature and thermal conductivity

Estimating the temperature of the hot spot is complicated by the fact that thermal conductivity (κ) is changing dynamically during the laser anneal. To quantify changes in κ within the resonators after the laser annealing process, we systematically vary the laser readout power (Fig. 2a) while monitoring the drums resonance frequency. This approach allows us to estimate κ since the resonance frequency changes due to an expansion or contraction of the film heated by the measurement beam. From the shape of the resulting frequency vs. measurement laser power curve, we can calculate κ. Fig. 6 shows the resulting dependence of f vs. laser readout power for two laser-annealed CMG domes and one "pure" graphite resonator (for reference). We find in all cases here that f initially increases, then decreases with increasing measurement power, which matches well with the general trend of graphite's thermal expansion coefficient (i.e., an initially negative α, increasing to a positive α with temperature) [33].

Because κ is low for the CMG resonators, they reach higher temperatures at lower laser readout powers and hence, we observe the "turn-over" point associated with the change in sign of α at low measurement powers (Fig. 6). Since graphite has a significantly higher κ (≥ 10–$100\times$) compared to CMG resonators, we do not observe the "turn-over" point in the plotted power range for the graphite resonator in Fig. 6. We use κ as a fitting parameter to match the position of the turn-over point and the shape of the $\Delta f/f_o$ peak (Eq. (5)). For CMG resonators annealed here using $P=1.7$ mW, we estimate κ at 18 W/mK, whereas using a $P=5.5$ mW anneal, κ increases to 43 W/mK. As a consistency check, we also estimate κ for the graphite resonator at 1800 W/mK, which is in excellent agreement with expected values [34].

Using these estimated thermal conductivities, we can calculate the temperature distribution within the suspended drums using FEM analysis (ANSYS software). Fig. 7 shows three examples of the calculated "hot spot" assuming different κ's (to be compared to the experiment in Fig. 5). During the 2D-rastered laser annealing process, the laser beam is always at the border between the already annealed (re-crystallized) part of the drum and the remaining, highly disordered part. As such, material properties such as κ change dynamically under the beam, causing the temperature distribution to be asymmetric. For κ of CMG films prior to the laser beam exposure we use a value $\kappa\approx 2$ W/mK, representative of disordered carbon films [34]. The model structure is a drum with $D=17.75$ μm and the heat source is assumed to be 1 mW of absorbed laser power. For a homogeneous $\kappa=20$ W/mK, the highest temperature occurs when the heat source is just outside the center hole and is estimated at $T\approx 1200$ K (Fig. 7a). Fig. 7b shows a calculation with inhomogeneous κ; $\kappa=2$ W/mK in the upper half of the drum (i.e., unannealed material) and $\kappa=20$ W/mK the lower half (i.e., after laser anneal). The resulting temperature distribution is skewed

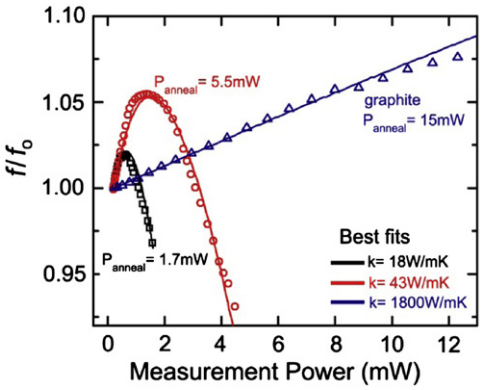

Fig. 6. (Color online) Plot of the normalized resonance frequency (f/f_o) vs. laser measurement power for two laser-annealed CMG resonators and one graphite resonator. All resonators were first laser annealed up to a given power (e.g., 1.7 mW), then the measurement power was increased up to the laser anneal power (i.e., 1.7 mW) so as not to modify the material with the measurement beam. The thermal conductivity is labeled for each of the best fits. The graphite resonator ($h=30$ nm, $D=6.5$ μm) was formed by mechanical exfoliation on pre-patterned SiO_2/Si.

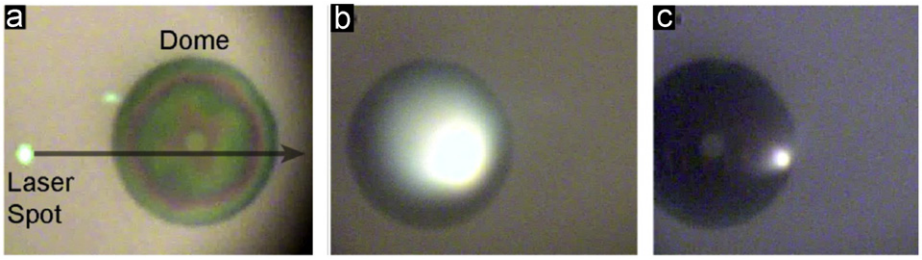

Fig. 5. (Color online) Screen shots taken from a movie of the laser spot moving across a dome resonator ($D\approx 20$ μm): (a) image before the laser moves on the drum and before the notch filter was inserted to remove all reflected light at 532 nm wavelength (this notch filter makes the laser beam invisible without affecting the general color balance). (b) Image when the laser spot is approximately 3 μm from the center. The white light is thermal radiation. (c) Image when the laser spot is approximately 8 μm from the center. The laser power is ~ 3 mW at the sample.

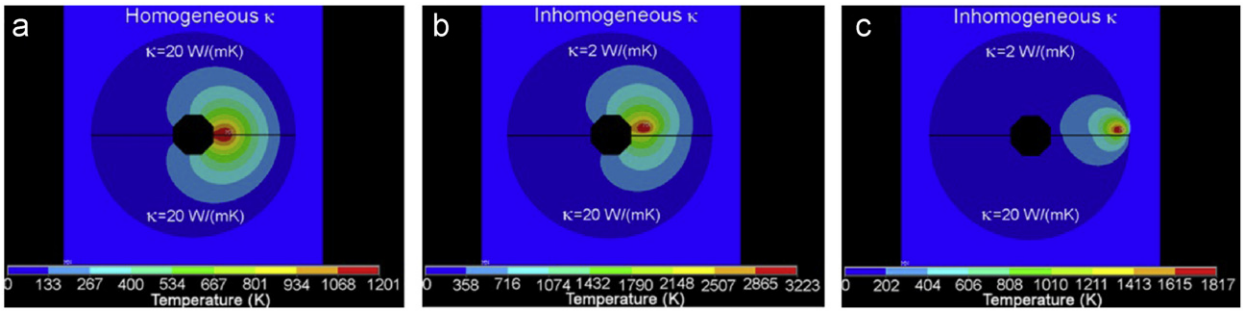

Fig. 7. (Color online) ANSYS calculations of the temperature distribution on a thin suspended membrane with a hole in the center and a one-micron heat source (D=17.75 μm, h=20 nm): (a) calculations preformed with a homogeneous thermal conductivity (κ) of 20 W/mK, with the hot spot centered at 3 μm from the center. (b) Calculations with an inhomogeneous κ—the upper half of the drum has κ=2 W/mK and the lower half has κ=20 W/mK. The hot spot is centered 3 μm from the center. (c) Calculations with an inhomogeneous κ—the upper half of the drum has κ=2 W/mK and the lower half has κ=20 W/mK. The hot spot is centered at 8 μm from the center.

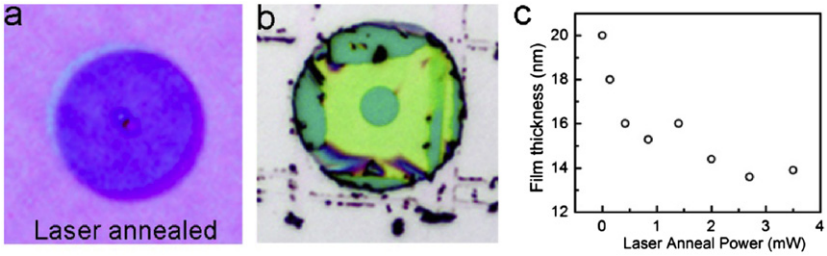

Fig. 8. (Color online) (a) Nomarski optical microscope (OM) image of a ~20 μm dome resonator after laser annealing. This should be compared to the dome in Fig. 4c inset. (b) OM image of a crashed membrane (D=20 μm). (c) Plot of resonator thickness vs. laser anneal power, measured at the center hole shown in (b).

toward the upper half of the drum with the hottest spot at $T \approx 3200$ K, which we believe represents an upper temperature bound since re-crystallization would rapidly occur at such temperatures, resulting in increased κ and drop in temperature. Finally, Fig. 7c shows how the hot spot changes when the beam is close to the drum edge with an inhomogeneous κ (i.e, half-annealed drum). Notably, these calculated results are in relatively good agreement with the qualitative trend found in experiment (Fig. 5), and suggest the highest local temperatures may instantaneously reach $T \approx 3200$ K.

5.5. Morphology: Graphene "Shrink wrap"

To characterize re-crystallization processes that give rise to new microstructures within the resonators, we start with domes (Fig. 4c inset) for which Young's modulus (Fig. 4d) and thickness (Fig. 8) are known. Exposing these domes to even low laser powers ($P > 200$ μW) causes the suspended film to snap flat as shown in Fig. 8a (to be compared to Fig. 4c inset). This transition from a relaxed dome to a highly tensioned membrane reflects profound structural changes within the film. To quantify how film density might be changing, we measure the thickness of different domes before and after laser annealing. By intentionally crashing the resonators (after laser annealing) so they lie flat on the substrate, we can use AFM to measure the step height at the lithographically-defined irrigation hole originally used for fabrication (Fig. 8b). For a 1 mW laser anneal the change in resonator thickness (Δh) is ~20% and for a 3.5 mW anneal Δh is ~40% (Fig. 8c). Assuming no carbon atoms are lost during treatment, the corresponding increase in density from thermally annealed domes ($\rho \approx 1.8$ g/cm^3) would be $\rho \approx 2.2$ g/cm^3 and $\rho \approx 2.5$ g/cm^3, respectively. The density of $\rho \approx 2.5$ g/cm^3 likely represents an upper bound as some carbon atoms would leave with any residual O or F adsorbates, whose remaining concentration is less than 15 at%.

5.6. Bonding structure and modulus

While structural changes induced by laser annealing are suggested by variations in film morphology and density, they are more directly monitored using Raman spectroscopy. Raman is a powerful tool for characterizing sp^2-carbon materials, even down to atomically thin layers [35]. Before laser annealing, CMG resonators have broad D (~1350 cm^{-1}) and G (~1600 cm^{-1}) peak similar to that found in GO [36] or highly disordered graphitic films [37] (Fig. 9a, "0 mW"). At low laser annealing powers (e.g., "1.7 mW", Fig. 9a) there is a further broadening of the D and G peaks, suggesting a further decrease in sp^2 content. This trend reverses at moderate powers (e.g., 7 mW), where there is a distinct narrowing of the D and G peaks, an increase in the G/D peak ratio, and the emergence of the 2D peak (~2700 cm^{-1}). Somewhat surprisingly, at the highest powers (e.g., 18.9 mW) the resonators transition to nearly defect-free turbostratic graphite, as observed by the disappearing D peak and single-Lorentzian 2D peak.

A schematic representation of the possible micro-structural transformation is shown in Fig. 9b and c. Initially, the resonator density is at its lowest and sp^2 defects are most likely associated with residual functional groups (oxygen and fluorine), vacancies/edges, or dangling bonds (blue spots in Fig. 9d). Low-power laser annealing further induces sp^3-carbon bonding as functional groups desorb and bonds rearrange into meta-stable configurations resulting in direct platelet–platelet bonding (red spots in Fig. 9c). This re-crystallization also corresponds to a decrease in film thickness (Fig. 8c), and increase in film resilience and film modulus (discussed below). At the highest annealing powers there is enough energy to transform carbon into its most thermodynamically favorable state of well-ordered sp^2-bonded carbon (Fig. 9b).

A significant increase in film stiffness associated with laser annealing further confirms the structural reinforcement provided by platelet–platelet bonding. To measure Young's modulus of

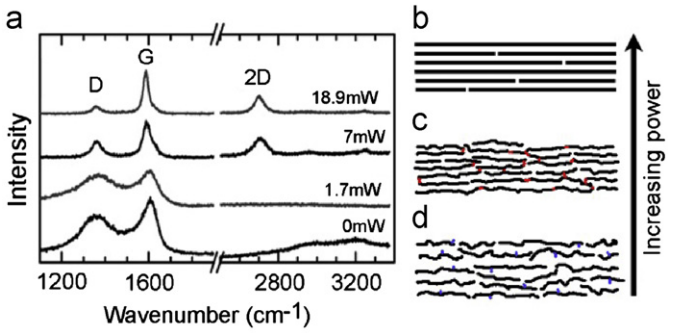

Fig. 9. (Color online) (a) Raman spectra from drum resonators treated with different laser powers (powers labeled on right; adapted from [11]). (b)–(d) Cartoon schematic illustrating the possible film microstructure after different laser treatments. The blue spots in (d) represent residual functional groups, while the red spots in (c) represent newly formed platelet–platelet bonds.

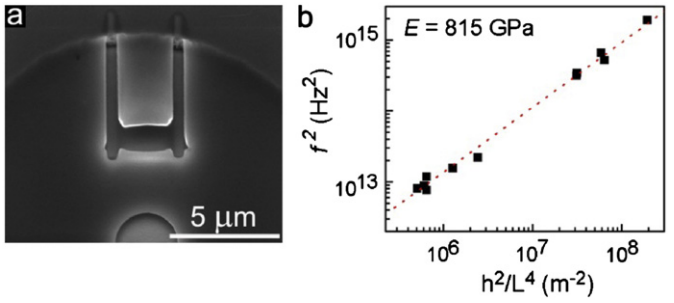

Fig. 10. (Color online) (a) SEM image of a FIB micro-machined cantilever from a laser annealed resonator. (b) Plot of f^2 vs. h^2/L^4 Eq. (4) from which Young's modulus (E) is extracted (adapted from [11]).

laser annealed suspended films, we use a FIB to cut cantilevers out of laser-treated drum resonators. Fig. 10a shows an example of one such resonator. By fabricating and measuring cantilevers of varying lengths we can use Eq. (4) to extract E. Fig. 10b shows a plot of f^2 vs. h^2/L^4 and the resultant slope is used to calculate $E=815\pm14$ GPa, a remarkable $14\times$ increase over the starting films (Fig. 4d) despite the small sp^2-crystalline size (Fig. 9a). Amazingly, the initial paper mache-like film now has a modulus close to that of diamond.

5.7. Film resilience

An increase in inter-platelet interactions in randomly assembled multi-layer CMG films should be evident in stress relaxation experiments. As described earlier, thermally treating CMG resonators between 300 and 450 °C resulted in complete resonator relaxation and the formation of dome-like structures (Figs. 3b and 4c). Such relaxation indicates relatively weak platelet–platelet bonding. However, this is not the case for laser re-crystallized resonators. Fig. 11 shows the normalized stress for resonators (laser annealed at different powers) after extended thermal annealing at 450 °C. Non-laser-annealed resonators relax almost immediately (within 5 min), while re-crystallized resonators can maintain 80% of their initial stress even after annealing for >5 h. We find the peak stress attainable after laser annealing can be as high as 1 GPa [11], which provides a lower bound for the room temperature strength of the films.

The rheology of platelet-based films primarily depends on the inter-platelet interactions and can vary with temperature due to different activation energies of the interacting elements, resulting in a spectrum of relaxation times. Such systems can be phenomenologically described using the stretched-exponential relaxation (SER) function, $\exp[-(t/\tau)^{\beta}]$, where τ is a material sensitive

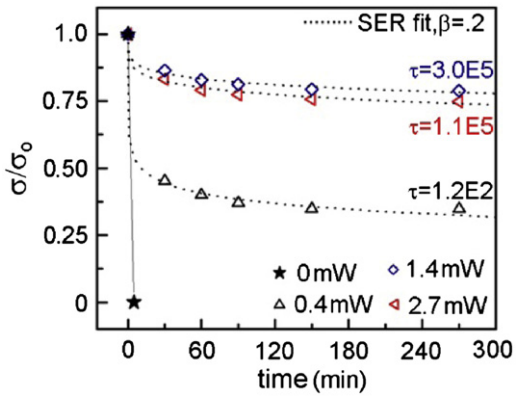

Fig. 11. (Color online) Normalized stress ($\sigma/\sigma_o=f^2/f_o^2$, Eq. (2)) as a function of time for an extended anneal at $T=450$ °C, following laser anneal (laser powers labeled). The dashed lines are the best fit stretched exponential relaxation (SER) function with $\beta=0.2$. The time constant (τ) for each curve is labeled.

parameter useful for discussing chemical trends [38] and β is the shape parameter ($0<\beta<1$). Here we show a good fit occurs when applying the SER function to the data in Fig. 11 using a $\beta=0.2$. We view the deviation from a simple exponential dependence ($\beta=1.0$) as an indication of an increasingly crosslinked microstructure [38].

5.8. Engineering nanomechanical performance

Until now we have focused on characterizing mechanical or thermal properties (e.g., strain, modulus, thermal conductivity, etc.) of multilayer graphene-based thin films from the dynamic response of the nanomechanical resonators. From an engineering perspective, one would like to tune the film properties in a way that will produces the highest performance for a given nanomechanical device. The resonators themselves serve as a fine example of a system where the figure-of-merit is directly affected by the film properties. In applications like mass sensors or signal processing, it is a combination of the frequency range and quality factor (Q) that largely determine the critical parameters like mass sensitivity [39] or clock's phase noise [40]. By employing chemical and structural modifications within graphene-based films, the NEMS designer can tune the fundamental frequency through in-plane tension.

The altered spring constant (k_s) affects the quality factor (Q) by changing the total energy (W_{total}) stored in the resonator, since $Q=W_{total}/W_{dissipation}$ ($W_{dissipation}$=total dissipated energy per cycle). The W_{total} is dependent on the resonator's stiffness ($W_{total}=k_sX^2/2$ in a simple "mass on a spring" model, where X is displacement). In the absence of viscous losses (e.g., operated in vacuum) and with negligible clamping losses, the $W_{dissipation}$ is defined by the internal friction (Q^{-1}) of the CMG film and can be affected by both intra-platelets defects, as well as inter-platelet crosslinks. Therefore, one would expect the laser re-crystallization process to affect the resonator Q-values in two different ways (i.e., through k_s and $W_{dissipation}$).

Fig. 12 shows the trends in resonance frequency vs. quality factor for different laser annealing powers for a particular laser-annealed drum resonator ($D=20$ μm). Assuming that the total mass of the resonator is unaltered during laser annealing, the square of the fundamental frequency (f_0^2) is proportional to k_s of the drum. The linear increase of the quality factor for Q vs. f^2 at low laser power (Region I, 0.04 mW $<P<$ 0.6 mW, Fig. 12a) can be attributed mainly to increased tension (or k_s). However, annealing at powers between 0.6 mW $<P<$ 1.7 mW (Region II),

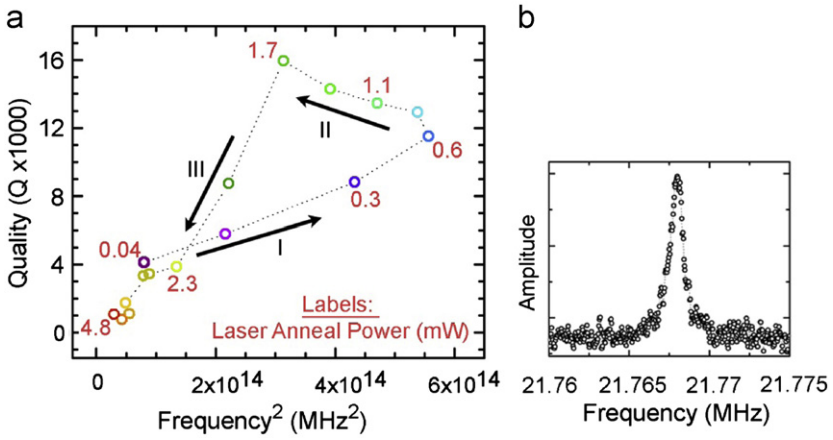

Fig. 12. (Color online) (a) Effect of laser annealing on resonator quality factor and spring constant ($k_s \sim f^2$). The drum resonator ($D=20$ μm) was released by XeF_2 gas etch, thermally annealed at 450 °C to form a dome, and then sequentially laser-annealed with increasing laser power. The laser power (Nd:YAG, 532 nm) associated with a particular data point is specified in the figure and also color coded (with purple corresponding to the lowest laser power and red color used for the highest laser power). (b) Plot of amplitude vs. frequency for a resonator with RT quality factor of 31,000 (adapted from [11]).

the spring constant *decreases* while Q *increases*. Such an increase in Q with decreasing W_{total} can only occur by reducing $W_{dissipation}$. The formation of inter-platelet cross-links is a leading candidate as a mechanism that improves film integrity (i.e., diminished losses) in Region II. Thus, the peak quality factor $Q \sim 16{,}000$ in Fig. 12a (1.7 mW laser anneal) should be attributed to both high residual tensile stress, as well as a refined microstructure. Raman spectra from these highest Q resonators consistently have the broadest D and G peaks, emphasizing the needed increase in sp^3 C content to improve mechanical performance. After reaching the maximum Q, the quality factor decreases with increasing laser power (Region III). The linear dependence of Q vs. f^2 suggests a decrease in tension as a main factor affecting Q in Region III.

The highest $Q \approx 31{,}000$ (Fig. 12b) observed in this work is amongst the best performance for a thin-film (i.e., flexural mode) carbon-based resonator at room temperature. We view an order-of-magnitude improvement in quality factor of CMG drums over CVD-grown pristine graphene resonators [41] as a direct outcome of CMG tunability, which allowed us to balance cross-stitching within the CMG film and to maximize the tensile stress. Further optimization of Q could be provided by a variable-power laser anneal that compensates for the strong heat sink at the periphery of the drum (e.g., Fig. 5c), ensuring a homogeneous anneal across the suspended film.

6. Outlook and summary

We view the results presented here as further support that randomly assembled films of carbon platelets are an ideal "raw" material, which can be re-shaped and/or re-structured into thin film systems otherwise unattainable. In multilayer graphene, this includes transforming layered sp^2 carbon into hybrid sp^2–sp^3 inter-bounded materials. The availability of wafer scale, atomically thin films that can be deposited from solution (e.g., by simple spin casting) and that have mechanical properties akin to diamond-like carbon will greatly benefit numerous NEMS devices, from resonators to semi-permeable membranes (e.g., molecular sieves). We envision new applications such as nano shrink-wrap or nano-muscle, enabled by the local control over chemical and structural CMG transformations. Developing such control will require a detailed understanding of pathways that link different sp^2–sp^3 hybridization states. As an example, such understanding will define the ultimate limit in thickness for CMG films that are transformable into diamond or diamond-like carbon. A system of few-layer stacked graphene is an emerging topic of interest [42]. Towards this end, we are developing techniques applicable to few-layer graphene films (Fig. 13).

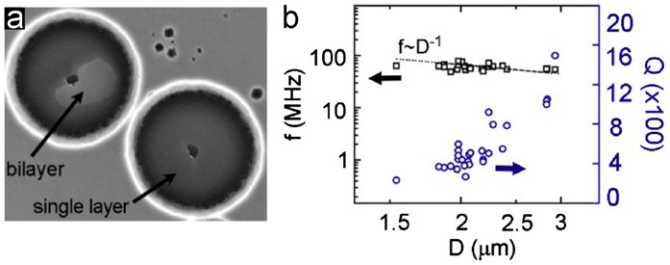

Fig. 13. (Color online) (a) SEM image of CVD-grown graphene drum resonators ($D \approx 1.5$ μm). (b) Plot of f and Q versus drum diameter (D) for a series of resonators as shown in (a).

In summary, we use the response of the lithographically-defined nanomechanical devices to show the effect of adsorbates, defects, and re-crystallization on the mechanical properties of multilayer graphene-based films. Laser irradiation and re-crystallization of suspended CMG produces a 3D-networked material with greatly improved strength (sustainable stresses up to 1000 MPa), Young's modulus ($E=815$ GPa) and quality factors ($Q=31{,}000$ at RT). In our view, a chemistry-based toolbox for tuning mechanics is an enabling technique to make graphene a true nanomechanical "material-by-design".

Acknowledgments

The authors are grateful for funding from the Office of Naval Research and NRL's Nanoscience Institute. We thank David Zapotok and Dean St. Amand in NRL's Nanoscience Institute for continual technical support. We thank J.W. Baldwin and Z. Wei for assistance in material synthesis and resonator measurement. R.S. is an employee of Nova Research, Inc., Alexandria, VA.

References

[1] A. Hirsch, Nat. Mater. 9 (2010) 868–871.
[2] E.S. Snow, J.P. Novak, P.M. Campbell, D. Park, Appl. Phys. Lett. 82 (2003) 2145–2147.

[3] E.S. Snow, F.K. Perkins, E.J. Houser, S.C. Badescu, T.L. Reinecke, Science 307 (2005) 1942–1945.
[4] W.R. Michael, A.T. Mark, D.M. Michael, P. Hans-Jurgen, D. Gilles, S. Niyazi Serdar, H. Liangbing, G. George, Appl. Phys. Lett. 88 (2006) 233506.
[5] G. Eda, G. Fanchini, M. Chhowalla, Nat. Nano 3 (2008) 270–274.
[6] X. Wang, L. Zhi, K. Mullen, Nano Lett. 8 (2007) 323–327.
[7] J.T. Robinson, F.K. Perkins, E.S. Snow, Z. Wei, P.E. Sheehan, Nano Lett. 8 (2008) 3137–3140.
[8] D.A. Dikin, S. Stankovich, E.J. Zimney, R.D. Piner, G.H.B. Dommett, G. Evmenenko, S.T. Nguyen, R.S. Ruoff, Nature 448 (2007) 457–460.
[9] J.T. Robinson, M. Zalalutdinov, J.W. Baldwin, E.S. Snow, Z. Wei, P. Sheehan, B.H. Houston, Nano Lett. 8 (2008) 3441–3445.
[10] S.H. Lee, H.W. Kim, J.O. Hwang, W.J. Lee, J. Kwon, C.W. Bielawski, R.S. Ruoff, S.O. Kim, Angew. Chem. Int. Ed. 49 (2010) 10084–10088.
[11] M.K. Zalalutdniov, J.T. Robinson, C.E. Junkermeier, J.C. Culbertson, T.L. Reinecke, R. Stein, P.E. Sheehan, B.H. Houston, E.S. Snow, Nano Lett., 12 (2012) 4212–4218.
[12] K.S. Novoselov, A.K. Geim, S.V. Morozov, D. Jiang, Y. Zhang, S.V. Dubonos, I.V. Grigorieva, A.A. Firsov, Science, 306 (2004) 666–669.
[13] S. Stankovich, R.D. Piner, X. Chen, N. Wu, S.T. Nguyen, R.S. Ruoff, J. Mater. Chem. 16 (2006) 155–158.
[14] A. Reina, X. Jia, J. Ho, D. Nezich, H. Son, V. Bulovic, M.S. Dresselhaus, J. Kong, Nano Lett. 9 (2008) 30–35.
[15] Y. Qingkai, L. Jie, S. Sujitra, L. Hao, P.C. Yong, P. Shin-Shem, Appl. Phys. Lett. 93 (2008) 113103.
[16] X. Li, W. Cai, J. An, S. Kim, J. Nah, D. Yang, R. Piner, A. Velamakanni, I. Jung, E. Tutuc, S.K. Banerjee, L. Colombo, R.S. Ruoff, Science (2009) 1171245.
[17] C. Berger, Z. Song, T. Li, X. Li, A.Y. Ogbazghi, R. Feng, Z. Dai, A.N. Marchenkov, E.H. Conrad, P.N. First, W.A. de Heer, J. Phys. Chem. B 108 (2004) 19912–19916.
[18] S. Bae, H. Kim, Y. Lee, X. Xu, J.-S. Park, Y. Zheng, J. Balakrishnan, T. Lei, H. Ri Kim, Y.I. Song, Y.-J. Kim, K.S. Kim, B. Ozyilmaz, J.-H. Ahn, B.H. Hong, S. Iijima, Nat. Nano 5 (2010) 574–578.
[19] J.T. Robinson, J.S. Burgess, C.E. Junkermeier, S.C. Badescu, T.L. Reinecke, F.K. Perkins, M.K. Zalalutdniov, J.W. Baldwin, J.C. Culbertson, P.E. Sheehan, E.S. Snow, Nano Lett. 10 (2010) 3001–3005.
[20] B. Ilic, S. Krylov, K. Aubin, R. Reichenbach, H.G. Craighead, Appl. Phys. Lett. 86 (2005) 193114.
[21] J.S. Bunch, A.M. van der Zande, S.S. Verbridge, I.W. Frank, D.M. Tanenbaum, J.M. Parpia, H.G. Craighead, P.L. McEuen, Science 315 (2007) 490–493.
[22] P.M. Morse, K.U. Ingard, Bars, membranes, and plates, Theoretical Acoustics, Princeton University Press, Princeton, NJ, 1968, pp. 209–211.
[23] P.M. Morse, K.U. Ingard, Bars, membranes, and plates, Theoretical Acoustics, Princeton University Press, Princeton, NJ, 1968, pp. 213–216.
[24] P.M. Morse, K.U. Ingard, Bars, membranes, and plates, Theoretical Acoustics, Princeton University Press, Princeton, NJ, 1968, pp. 181–182.
[25] W. Bao, F. Miao, Z. Chen, H. Zhang, W. Jang, C. Dames, C.N. Lau, Nat. Nano 4 (2009) 562–566.
[26] I. Finnie, W. Heller, McGraw-Hill Book Company, Inc., New York, Toronto, London, 1959, p. 38, 120.
[27] X. Liu, T.H. Metcalf, J.T. Robinson, B.H. Houston, F. Scarpa, Nano Lett. 12 (2012) 1013–1017.
[28] J.D. Brazzle, M.R. Dokmeci, C.H. Mastrangelo, in: 17th IEEE International Conference on Micro Electro Mechanical Systems, 2004 (MEMS), 2004, pp. 737–740.
[29] C. Gomez-Navarro, J.C. Meyer, R.S. Sundaram, A. Chuvilin, S. Kurasch, M. Burghard, K. Kern, U. Kaiser, Nano Lett. 10 (2010) 1144–1148.
[30] R.H. Telling, C.P. Ewels, A.A. El-Barbary, M.I. Heggie, Nat. Mater. 2 (2003) 333–337.
[31] A. Bagri, C. Mattevi, M. Acik, Y.J. Chabal, M. Chhowalla, V.B. Shenoy, Nat. Chem. 2 (2010) 581–587.
[32] J. Kotakoski, A.V. Krasheninnikov, U. Kaiser, J.C. Meyer, Phys. Rev. Lett. 106 (2011) 105505.
[33] N. Mounet, N. Marzari, Phys. Rev. B 71 (2005) 205214.
[34] A.A. Balandin, Nat. Mater. 10 (2011) 569–581.
[35] A.C. Ferrari, J.C. Meyer, V. Scardaci, C. Casiraghi, M. Lazzeri, F. Mauri, S. Piscanec, D. Jiang, K.S. Novoselov, S. Roth, A.K. Geim, Phys. Rev. Lett. 97 (2006) 187401.
[36] S. Stankovich, D.A. Dikin, R.D. Piner, K.A. Kohlhaas, A. Kleinhammes, Y. Jia, Y. Wu, S.T. Nguyen, R.S. Ruoff, Carbon 45 (2007) 1558–1565.
[37] A.C. Ferrari, J. Robertson, Phys. Rev. B 61 (2000) 14095–14107.
[38] J.C. Phillips, J. Non-Cryst. Solids 357 (2011) 3853–3865.
[39] J.L. Arlett, E.B. Myers, M.L. Roukes, Nat. Nano 6 (2011) 203–215.
[40] L. Seungbae, C.T.C. Nguyen, in: Frequency Control Symposium and Exposition, 2004. Proceedings of the 2004 IEEE International, 2004, pp. 144–150.
[41] R.A. Barton, B. Ilic, A.M. van der Zande, W.S. Whitney, P.L. McEuen, J.M. Parpia, H.G. Craighead, Nano Lett. 11 (2011) 1232–1236.
[42] R. Ruoff, Nature 483 (2012), S42-S42.